Anomalous Magneto-Optical Effects in an Antiferromagnet–Topological-Insulator Heterostructure

Amrit De,[*,§] Tonmoy K. Bhowmick,[†,§] and Roger K. Lake[‡]
Department of Electrical Engineering, University of California Riverside, California 92521, USA

(Received 20 June 2020; revised 5 May 2021; accepted 13 May 2021; published 16 July 2021)

We show that large magneto-optic Kerr effects (MOKEs) emerge when an antiferromagnet (AFM) is proximately coupled to a topological insulator (TI) film—where neither the perfect collinear Néel ordered single-domain AFM nor the unmagnetized TI individually shows any MOKE. Because of the lack of macroscopic magnetization, the AFM only couples to the spin of one of the TI's surfaces breaking time-reversal and inversion symmetry—which leads to a small microdegree MOKE signal. This small MOKE can be easily enhanced by 5 orders of magnitude, via cavity resonance, by optimizing the AFM and TI film thicknesses on the substrate. For slightly off-resonant structures, a 6° Kerr rotation can be electrically switched on by varying the Fermi energy. This requires less than 20 meV, which is encouraging for low-power spintronics and magneto-optic devices. We further show that this simple structure is easily resilient to 5% material growth error.

DOI: 10.1103/PhysRevApplied.16.014043

I. INTRODUCTION

The Faraday effect and the magneto-optic Kerr effect (MOKE) can be viewed as optical manifestations of the Berry curvature. The optical response functions in the MOKE are analogous to those of electrical Hall conductivity. However, there are subtle differences and additional probing capabilities due to the inter- and intraband transitions, interface effects, and frequency and directional dependencies. These properties lead to magneto-optic (MO) effects in quantum Hall devices [1,2], quantum materials such as topological insulators (TIs) [3–5], magnetized chiral systems [6], and skyrmions [7–11]. Magneto-optic effects are useful for device applications [12,13]. Optical isolators exploit the Faraday effect, and the polar MOKE is used to optically read out magnetically stored information [14–16]. Even with large macroscopic magnetizations, the Kerr rotation tends to be small—barely 1°, for most MO materials [17–22]. Some exceptions such as CeSb [23] rely on resonance effects from the hetrostructure.

The MOKE requires broken time-reversal symmetry (TRS). Strongly magnetized materials, such as ferromagnets (FMs), show large MOKEs, but they also have large stray magnetic fields that are undesirable for devices. Antiferromagnets (AFMs) are more attractive since they have smaller stray fields and also electrically switch much faster than FMs [24–26]. The Néel ordering in a *perfect single-domain* collinear *g*-type AFM generally cannot result in a *polar* MOKE, since the spin compensation on the two sublattices would give zero net magnetization. An *a*-type or *e*-type AFM could show a nonlinear MOKE from its surface. Experimentally observed MOKE in AFMs is typically attributed to domain walls [27], residual Dzyaloshinskii-Moriya interactions [27–29], residual Berry phases [30,31], magnetic octupole moments [31–33], spin canting [34], crystal chirality [35], and stray magnetization [27,36]. Similarly, an ideal TI that preserves TRS should not show a linear MOKE, although approximately microdegree Faraday rotations from a TI's surface were recently detected using nonlinear magneto-optics and circularly polarized pumps [37]. Observing MOKEs in TIs generally requires either external magnetic fields [3,4], magnetic doping [38], or proximity coupling to materials with net magnetization [11,39]. In this paper we show that a MOKE signature arises at the interface of a TI and a collinear *g*-type AFM. This MOKE signature can be enhanced by 5 orders of magnitude, to $1^\circ - 2^\circ$, by using resonant enhancements from the structure and small electric fields. This strong anomalous MOKE occurs in the absence of external magnetic fields, stray magnetic moments, or magnetic dopants.

The MOKE in this system is a result of the breaking of symmetries that allow MOKE and the anomalous Hall effect in noncollinear AFMs with no net magnetic moments and the predicted voltage-controlled MOKE in a collinear AFM [40]. In a three-dimensional TI, TRS is preserved, and the degenerate Kramers pairs of the surface states exist on opposing surfaces. In a *g*-type AFM,

*amritde@gmail.com
†tbhow001@ucr.edu
‡rlake@ece.ucr.edu
§These authors contributed equally.

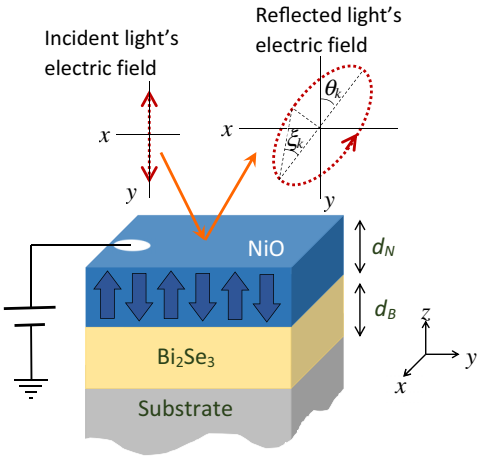

FIG. 1. MOKE from a thin-film collinear antiferromagnet on top of a thin-film topological insulator. We specifically consider a NiO film on a Bi_2Se_3 thin film grown on a SiO_2 substrate.

TRS is broken by the opposing spin alignments on its bipartite lattice, and, macroscopically, there is no net magnetization. Proximally coupling the AFM to one surface of the TI breaks both TRS and inversion symmetry, and this allows the system to exhibit a nonzero MOKE with no net magnetic moment.

In this paper, we specifically consider a heterostrcuture as illustrated in Fig. 1 with material parameters corresponding to a NiO film (AFM) grown on a Bi_2Se_3 film (TI) deposited on a SiO_2 substrate. The resulting Kerr rotation from a TI single surface is tiny (of the order of microdegrees) as expected. However huge enhancements, resulting in a 5-order-of-magnitude increase in the MOKE, are shown to arise by carefully choosing the film thicknesses of NiO and Bi_2Se_3. The NiO layer and the SiO_2 substrate form a cavity, which can boost the MOKE via cavity resonance effects [23]. The resonant optical frequency is film thickness dependent. We further show that Kerr rotations of over 5° can be obtained by electrically biasing slightly detuned structures. In general, expected film growth errors will naturally detune the MOKE resonance. We show that for ±5% film-thickness errors, even in the worst case, Kerr rotations of at least 1° can still be obtained by applying an electrical bias of under 20 meV. Overall this simple and practical TI/AFM device can generate a huge MOKE, while consuming very little power. It is planar, compact, and free of stray magnetic fields and external magnets. These features are very attractive for practical spintronic devices, sharp MO switches, MO memory, and electro-optics including optical isolators.

In the next section we discuss our model and the methods used in greater detail. This is followed by a discussion of the results and a summary.

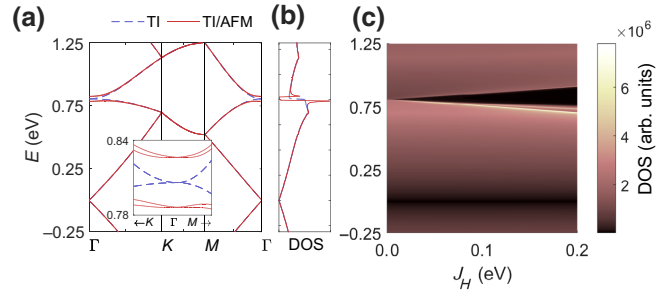

FIG. 2. (a) Band structure and (b) density of states (DOS) for TI only ($J_H = 0$, dashed blue line) and for TI/AFM ($J_H = 40$ meV, solid red line). The inset in (a) shows the higher energy gap and the Rashba-type dispersion that occur with $J_H = 40$ meV. (c) DOS as a function of J_H.

II. THE MODEL AND METHOD

The low-energy zone-center effective Hamiltonian for a thin-film TI [41,42] is $H_0(\mathbf{k}) = \tau_z h_D(\mathbf{k}) + m_k \tau_x$, where τ_z and τ_x are Pauli matrices, respectively representing the TI's top and bottom surfaces and the hybridization between them. $h_D(\mathbf{k}) = \hbar v(k_y\sigma_x - k_x\sigma_y)$ is the two-dimensional Dirac cone Hamiltonian with Fermi velocity v and $m_k = m_0 + m_1(k_x^2 + k_y^2)$ is the interlayer hybridization. We discretize this Dirac model and obtain the following tight-binding Hamiltonian for an AFM proximally coupled to a TI:

$$H = \sum_i \mathbf{c}_i^\dagger h_i \mathbf{c}_i + \sum_{\langle i,j\rangle} (\mathbf{c}_i^\dagger \mathbf{t} \mathbf{c}_j + \text{h.c.}) + J_H \sum_i \mathbf{c}_i^\dagger \boldsymbol{\sigma}_i' \cdot \mathbf{S}_i \mathbf{c}_i, \tag{1}$$

where $h_i = [m_0 + (4m_1/a^2)]\tau_x \otimes \sigma_0$, the site indices $\langle i,j\rangle$ run over all nearest-neighbor sites, and $\mathbf{c}_i = [c_{i,1,\uparrow}\ c_{i,1,\downarrow}\ c_{i,2,\uparrow}\ c_{i,2,\downarrow}]^T$ is the spinor annihilation operator for site i and layers 1 and 2. Here $t \in \{t_x, t_y\}$ represents nearest-neighbor hopping, where $t_{x(y)} = \pm(i\hbar v/2a)\tau_z \otimes \sigma_{y(x)} - (m_1/a^2)\tau_x \otimes I$. It is implied that $\boldsymbol{\sigma}' = I \otimes \boldsymbol{\sigma}$, where I is the identity, $\boldsymbol{\sigma} = \{\sigma_x, \sigma_y, \sigma_z\}$ is the Pauli spin vector for the TI's itinerant electron, and $\mathbf{S} = \{S_x, S_y, S_z\}$ is the spin vector of the AFM. The TI's surface spins interact with the AFM's spins via the Hund's rule coupling term J_H.

The electronic band structure [shown in Fig. 2(a)] and wave functions for the TI/AFM system are numerically calculated using a 2×2 supercell, where the Néel vector of the AFM texture is perpendicular to the TI's surface. The TI's top surface is proximally coupled to a G-type AFM thin film. We assume periodic boundary conditions along x and y. We set $m_0 = 6$ meV, $m_1 = 0.2$ eV Å^2, and $v = 0.5 \times 10^6$ m/s. The discretization length $a = 10$ Å and $J_H = 40$ meV. The Dirac cone is trivially gapped at Γ due to the $m(\mathbf{k})$ term, and this gap is unaffected by the proximity coupling to the AFM.

The proximity coupling of the G-type AFM to the TI has several effects. First, it increases the periodic unit cell from a single tight-binding site consisting of two surfaces and four spins to four tight-binding sites with two surfaces and 16 spins resulting in 16 bands. This doubling of the unit cell causes zone folding of the Brillouin zone resulting in crossing of bands at Γ at higher energies. The TI's proximity coupling to the AFM with $J_H = 40$ meV does not affect the low energy levels near the Dirac point. However a Rashba-type gap opens at the higher band crossing, as shown in Figs. 2(a) and 2(b), and this energy gap increases linearly with J_H as shown in Fig. 2(c). Since the bands are symmetric around $E = 0$, a similar gap also opens below the Fermi level. The gapping and Rashba-type dispersion at the higher band crossing results in singularities in the density of states on either side of the gap, as can be seen in Fig. 2(b). These bands, resulting from broken inversion symmetry, time-reversal symmetry, and zone folding, are then involved in the optical transitions that lead to the magneto-optic properties of this system.

A. Dielectric tensor components

Magneto-optic effects are determined by the dielectric tensor, which depends on the band structure and its topology. In particular for the polar Kerr effect considered here, the Néel vector of the AFM is along z, which is perpendicular to the surface and parallel to the optical incidence. The x and y directions preserve in-plane symmetry. The complex 3×3 dielectric tensor has $[\epsilon_{xx}, \epsilon_{yy}, \epsilon_{zz}]$ diagonal terms and off-diagonal ϵ_{xy} terms that are topology dependent.

The matrix elements of the optical conductivity tensor are obtained from the Kubo formula [43,44]:

$$\sigma_{\mu\nu} = \frac{ie^2}{hL} \int \frac{d^2k}{(2\pi)^2} \sum_{n,l} \frac{f_{nl}(\mathbf{k})}{\omega_{nl}(\mathbf{k})} \times \left(\frac{\Pi(\mathbf{k})^{\mu}_{nl} \Pi(\mathbf{k})^{\nu}_{ln}}{\omega - \omega_{nl}(\mathbf{k}) + i\gamma} + \frac{\Pi(\mathbf{k})^{\mu}_{ln} \Pi(\mathbf{k})^{\nu}_{nl}}{\omega + \omega_{nl}(\mathbf{k}) + i\gamma} \right), \quad (2)$$

where $\Pi^{\mu}_{nl}(\mathbf{k}) = \langle \psi_n(\mathbf{k}) | v_\mu | \psi_l(\mathbf{k}) \rangle$ is the matrix element of the velocity operator, $v_\mu = \partial H / \hbar \partial k_\mu$, where $\{\mu, \nu\} \in \{x, y\}$. The energy broadening parameter $\gamma = 17.5$ meV for all calculations. $\hbar\omega_{nl}(\mathbf{k}) = E_n(\mathbf{k}) - E_l(\mathbf{k})$ is the energy difference of an optical transition between an unoccupied band n and an occupied band l. $f_{nl}(\mathbf{k}) = f_n(\mathbf{k}) - f_l(\mathbf{k})$, where $f_n(\mathbf{k})$ is the Fermi factor; however, all calculations are performed at zero temperature. L is the thickness associated with the TI surface state taken to be 1 nm.

The velocity operator is similar to the Berry connection. For a single surface this leads to a momentum space gauge potential or an equivalent magnetic field. For a TI, the gauge fields for each surface cancel each other unless the symmetry between the top and bottom surfaces is broken, such as by an AFM on one side. The resulting MO effects can therefore be viewed as an optical manifestation of the Berry curvature.

Since an effective Hamiltonian has been used to obtain $\sigma_{\mu\nu}$, the missing higher band contributions are compensated for by adding a $\kappa/(\omega + i\gamma)$ term to the optical dielectric tensor as follows: $\epsilon_{\mu\nu}(\omega) = \varepsilon_o \delta_{\mu\nu} - (4\pi i/\omega)\sigma_{\mu\nu} - [\kappa/(\omega + i\gamma)]$, where ε_o is the vacuum permittivity. κ is adjusted so that the relative zero-frequency dielectric constant ϵ_0 (obtained from the optical sum rules) matches the known experimental value [45] for Bi_2Se_3.

For calculating the polar MOKE, the required complex in-plane refractive index is $n_\pm = \sqrt{\epsilon_\pm} = \sqrt{\epsilon_{xx} \pm i\epsilon_{xy}}$, where the $+$ $(-)$ sign represents right (left) circularly polarized [RCP (LCP)] light propagation. The complex MOKE is $\Theta_k = \theta_k + i\xi_k$, where the Kerr rotation and ellipticity, respectively, are

$$\theta_k = (\Delta_+ - \Delta_-)/2, \quad (3)$$

$$\xi_k = (|r_+| - |r_-|)/(|r_+| + |r_-|). \quad (4)$$

Since the eigenmodes here are LCP and RCP, the Kerr rotation angle can be expressed as the phase difference between these two modes. The complex phase $\Delta_\pm$ is in turn obtained from the Fresnel reflection coefficients $r^\pm = |r^\pm| \exp(-i\Delta_\pm)$. The observed reflective intensity is $R_\pm = |r^\pm|^2$. The MOKE in a multilayer thin-film structure can be significantly altered by internal reflection at various interfaces. At normal incidence, $r^\pm$ for N thin films can be calculated using a 2×2 characteristic matrix method [11,46] in the LCP/RCP eigenmode basis:

$$\mathbf{S}^\pm = \prod_{j=0}^{N} \frac{1}{t^\pm_{j,j+1}} \begin{bmatrix} 1 & r^\pm_{j,j+1} \\ r^\pm_{j,j+1} & 1 \end{bmatrix} \begin{bmatrix} e^{i\beta^\pm_{j+1}} & 0 \\ 0 & e^{-i\beta^\pm_{j+1}} \end{bmatrix}, \quad (5)$$

where $\beta_j = (2\pi/\lambda) n_j d_j$ is a phase factor, d_j is the thickness of the jth layer, and λ is the optical wavelength. The Fresnel reflection and transmission coefficients at normal incidence for each interface, respectively, are $r^\pm_{j,j+1} = (n^\pm_j - n^\pm_{j+1})/(n^\pm_j + n^\pm_{j+1})$ and $t^\pm_{j,j+1} = (2n^\pm_j)/(n^\pm_j + n^\pm_{j+1})$. The resultant complex reflection coefficient is $r^\pm = S^\pm_{12}/S^\pm_{11} = |r^\pm| \exp(-i\Delta_\pm)$, where $S^\pm_{\mu\nu} \in \mathbf{S}^\pm$.

III. DISCUSSION

The calculated optical dielectric functions of the TI with and without the AFM layer are shown in Figs. 3(a) and 3(b). For the TI alone, the numerically calculated σ_{xy} is zero [approximately $\mathcal{O}(10^{-64})$—well below numerical precision]. Once an AFM is introduced on one side of the TI, the resulting σ_{xy} increases to $\mathcal{O}(10^{-6})$ Ω^{-1} m^{-2} as shown in Fig. 3(b). However, there is no change in the

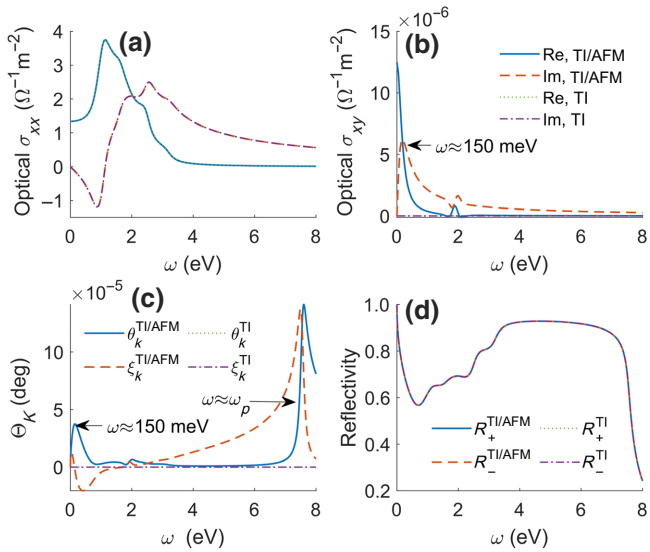

FIG. 3. Real and imaginary parts of the (a) diagonal and (b) off-diagonal optical conductivity for the TI alone and a coupled TI/AFM. Note that (a),(b) share the same legend. (c) Kerr rotation and ellipticity and (d) reflectivities for TI alone and for a single AFM/TI interface as denoted in the legend.

diagonal optical conductivity, σ_{xx}, as shown in Fig. 3(a). This is a significant result even though $\sigma_{xy} \ll \sigma_{xx}$.

These effects can be directly observed using MOKE. The resulting Kerr rotations, ellipticity, and reflectivities for the TI/AFM are shown in Figs. 3(c) and 3(d) for a single interface. The Kerr rotation features can be understood by examining the approximate expression for complex MOKE: $\Theta_k \approx \epsilon_{xy}/\left[\sqrt{\epsilon_{xx}}(1-\epsilon_{xx})\right]$ (since $\epsilon_{xy} \ll \epsilon_{xx}$) [47]. The MOKE resonance with $\theta_k \approx 4 \times 10^{-5\circ}$ occurs at $\omega(\theta_k^{\max}) \approx 150$ meV in the low-energy regime as shown in Fig. 3(c), which directly corresponds to the σ_{xy} peak in Fig. 3(b). There is also a high-energy MOKE resonance that occurs at 7.5 eV. Using the $1-\epsilon_{xx}$ resonance condition and the Drude model it can be shown that this is near the plasma frequency ω_p [11,48–51]. We extracted $\omega_p = 7.32$ eV from σ_{xy} using the optical sum rules [11]. Similarly, our extracted cyclotron frequency ω_c, from σ_{xy}, is 3.15 μeV, which is the effective ω_c of a single TI surface.

The MOKE can be enhanced by the resonance effects that arise from optimizing the film thickness of different materials. In order to understand the effects of this for our system, we consider a thin-film structure as shown in Fig. 1, where a NiO film of thickness d_N sits on a Bi_2Se_3 film of thickness d_B. The transfer matrices, Eq. (5), are used to calculate the MOKE spectra of the multilayer structures, assuming normal incidence and in-plane material isotropy. The optical dispersion relations for NiO are obtained from the literature [52]. The AFM/TI effects manifest themselves via $n_\pm$. The refractive index of air is used for the semi-infinite media above the NiO layer, and the dispersive refractive indices of SiO_2 are used for the semi-infinite substrate [53].

For the TI/AFM device, the Kerr rotation angle's phase diagram is shown in Fig. 4 as a function of ω, d_B, and d_N. The complete phase space is quite large. Therefore, representative phase diagrams are shown in Fig. 4 where one of the parameters is held constant and the other two are varied. In Figs. 4(a) and 4(b), d_B is held at 10 and 40 nm, respectively. The Kerr rotation angle θ_k has a considerable dependence on the NiO film thickness as it creates the resonances in the TI/AFM structure. For $d_B = 40$ nm, θ_k reaches 0.5° for $d_N \approx 1200$ nm. As shown in Fig. 4(c), with the NiO thickness fixed at its near-optimal value, a number of θ_k resonances begin to appear, with the highest peak being at Bi_2Se_3 thicknesses of about 40 nm at $\omega = 125$ meV. Note that the θ_k resonances occur at harmonics of ω, which is mainly dictated by d_N. Finally, with ω fixed at 125 meV, the θ_k phase diagram is shown in Fig. 4(d) as a function of d_N and d_B. A notable and sharp θ_k resonance happens at $d_N = 1162$ nm and $d_B = 37$ nm. The maximum Kerr rotation reaches 1.5° (for 1-Å thickness resolution)—an enhancement of 6 orders of magnitude compared with the value from the single surface. The ability to tune θ_k to exceed 1° is quite remarkable given that this is a purely anomalous MOKE that manifests in a collinear TI/AFM structure with no net magnetization and no external magnetic field.

Next, we analyze the Fermi-level-dependent MOKE spectra for the TI/AFM structure in Fig. 5. This phase diagram is particularly important for electro-optic device applications as it provides an electrical handle to control the anomalous magneto-optic effect in the TI/AFM.

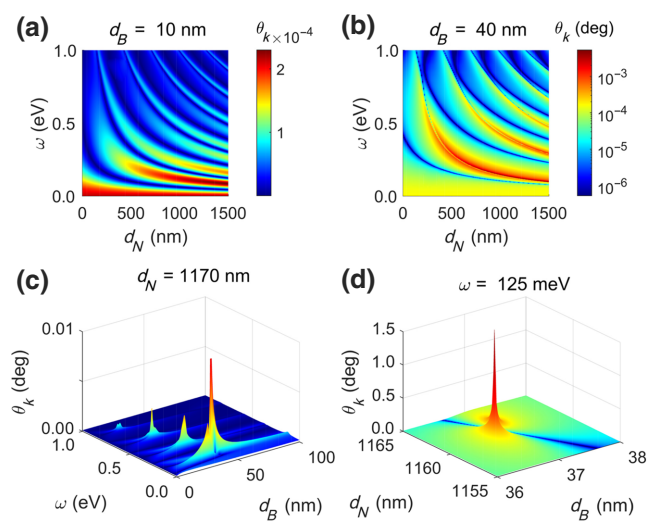

FIG. 4. The Kerr rotation (θ_k) phase diagram shown as a function of (a) d_N and ω for $d_B = 10$ nm, (b) d_N and ω for $d_B = 40$ nm, (c) d_N and ω for $d_B = 1.17$ μm, and (d) d_N and d_B at $\omega = 125$ meV.

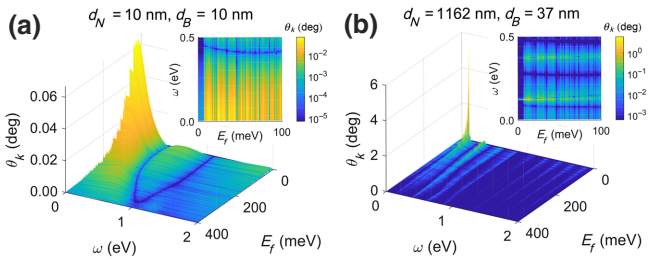

FIG. 5. The Kerr rotation angle as a function of Fermi energy E_f and optical frequency ω for (a) $d_B = 10$ nm and $d_N = 10$ nm and (b) $d_B = 1.16$ μm and $d_N = 100$ nm. The insets are enlargements to highlight the sudden switching behavior as a function of E_f.

θ_k is shown as a function of Fermi energy E_f and ω for two cases: $\{d_N, d_B\} = \{10, 10\}$ nm and $\{1162, 37\}$ nm. Although the {10,10}-nm case is not optimized, it is experimentally easier to grow, it is easier to electrically gate, and its physics is easier to explain even though the MOKE is quite weak. The second optimized thicker structure will have added cavity-induced resonance effects but with very strong MOKE. In Fig. 5(a), there is a sudden jump in θ_k when E_f crosses the band gap. As the Fermi level is further swept through the conduction band's Dirac cone, the number of optical transitions steadily decrease, which makes $\theta_k^{\max}$ shift to higher frequencies. These physical trends are further superposed on top of the strong cavity-induced resonances as shown in Fig. 5(b) for the $\{1162, 37\}$-nm structure. The MOKE resonances will only appear at optical harmonics as determined by the cavity (formed by NiO and the substrate). At $E_f = 7$ meV, $\theta_k \sim 6^\circ$ resonance occurs. This θ_k resonance is still over 4° by $E_f = 8$ meV.

We further analyze the MOKE spectra and the reflectivity for the two cases ($\{d_N, d_B\} = \{10, 10\}$ nm and $\{1162, 37\}$ nm) in Fig. 6. In addition we also examine the MOKE as a function of two different Fermi energies (E_f). The left (right) y axis of all panels in Fig. 6 is for $E_f = 0$ (optimal bias). Our choice of the optimal bias for each structure is based on the results of Fig. 7. As compared to the MOKE from the single TI/AFM interface shown in Fig. 3, the low-frequency peak in the Kerr rotation spectra is enhanced by 4 to 5 orders of magnitude by the resonance effects that arise from the thin-film thicknesses and interfaces. A number of subsequent smaller MOKE resonances appear at higher harmonics of the fundamental peak at $\omega = 125$ meV as expected. Maximum θ_k is also accompanied by a corresponding dip in the reflectivity. For the thinner films in Fig. 6(a), the MOKE decreases monotonically as a function of ω, as expected for the valance- and conduction-band states on the TI's Dirac cone. This monotonic behavior is absent for the thicker optimized $\{1162, 37\}$-nm TI/AFM structure as shown in Figs. 6(c) and 6(d). Instead, multiple MOKE spectral resonances

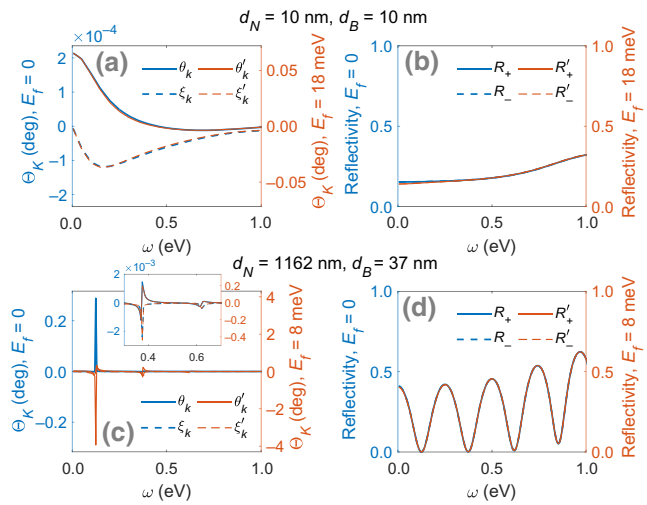

FIG. 6. (a) Kerr rotation and ellipticity and (b) the reflectivity spectra for $d_N = d_B = 10$ nm. (c) MOKE spectra and (d) reflectivity spectra for $d_N = 1162$ nm and $d_B = 37$ nm. The inset of (c) shows an expanded view of the smaller, higher-frequency resonances. The left (right) y axis of all the panels is for $E_f = 0$ ($E_f \neq 0$).

now appear at harmonics of ω that are resonant with the optical-cavity-like structure. The maximum Kerr rotation is around 0.3° in Fig. 6(c), for $E_f = 0$, after rounding off $\{d_N, d_B\}$ to the nearest nanometer. The frequency at which the maximum Kerr rotation occurs, $\omega(\theta_k^{\max})$, mainly shifts with d_N as shown in Fig.4(b). These resonantlike enhancements can still be observed for *growth errors* in layer thicknesses.

The Kerr angle θ_k can be sharply boosted by 1 to 3 orders of magnitude by applying a small bias to raise the Fermi energy in the TI/AFM, as shown in Fig. 6 (right-hand axis). For $E_F = 18$ meV, θ_k exceeds 0.05° for the nanometric thin films. Remarkably, θ_k reaches 4° for the thicker optimized structure with a small 8 meV bias. Ignoring the sign difference, the MOKE spectra also scale up uniformly in this

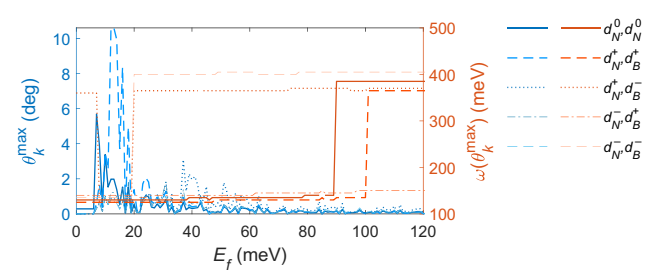

FIG. 7. (left-hand axis) The maximum Kerr rotation ($\theta_k^{\max}$) as a function of Fermi energy (E_f) for structures with no error and four combinations of $\pm 5\%$ error in the layer thickness. This thickness error is denoted by $d_{N(B)}^{\pm} = (1 \pm 0.05) \times d_{N(B)}^0$, where $\{d_N^0, d_B^0\} = \{1162, 37\}$ nm. (right-hand axis) The value of ω at which $\theta_k^{\max}$ occurs as a function of E_f.

small-bias regime with the $E_f = 0$ results in Fig. 6. The related reflectivity changes in Figs. 6(b) and 6(c) are quite small and not notable.

Finally, since thin-film growth can be prone to errors during the material deposition process, it is important to analyze how the TI/AFM device would behave with notable errors in the film thicknesses. In Fig. 7, the maximum Kerr rotation angle ($\theta_k^{\max}$) is shown as a function of Fermi energy with four combinations of $\pm 5\%$ error in the thickness of each layer. We assume that this error is homogeneous over the diffraction-limited spot size, since we use far-field plane-wave optics. Here $d_{N(B)}^{\pm}$ denotes $\pm 5\%$ deviation from the optimized $d_{N(B)}$. The right-hand axis in Fig. 7 shows the ω at which $\theta_k^{\max}$ occurs. Nominally, the Kerr rotation is nearly 6° at a 7-meV bias for the error-free case. While in the best case, a $+5\%$ homogeneous error in the layer thicknesses leads to an enhancement of the MOKE with $\theta_k^{\max} \approx 10^\circ$ with a 12- to 14-meV bias. For the worst case, $\theta_k^{\max}$ is about 1° with an 8-meV bias. This is very encouraging since a 1° Kerr rotation is still quite large. This shows that even with errors in layer growth near the resonance condition, it is still quite possible to observe a substantial anomalous MOKE signal by just electrically tuning the TI/AFM. In addition this is the basis of a very useful electro-optic device.

A notable feature is that $\omega(\theta_k^{\max})$ increases in a distinct steplike manner. The step size depends on the film thicknesses and can be explained from Fig. 5. The MOKE resonances only occur at higher harmonics of ω_r [where $\omega_r \equiv \omega(\theta_k^{\max})$ at $E_f = 0$]. As the Fermi level sweeps the Dirac-cone conduction band, $\theta_k^{\max}$ tends to shift to higher ω, due to steadily declining optical transitions. However, because of the thin-film structure, $\theta_k^{\max}$ can only jump to a higher harmonic of ω_r as shown in Fig. 5(b), which leads to the $\omega(\theta_k^{\max})$ steps in Fig. 7.

Much like the quantum Hall effect, the MOKE discussed in this paper should be topologically robust and largely insensitive to localized chemical defects, strain, pinning centers, etc. The MOKE ranges over the approximately $\mathcal{O}(\mu\text{m})$ diffraction-limited optical spot size, which is much larger than the lattice spacing or localized defects. A larger number of chemical defects and the lattice strain at the interface will perturb the band structure, which will in turn perturb the dielectric properties and the refractive indices. As a result the MOKE resonances might spectrally shift, but would still remain observable.

IV. SUMMARY

In summary, the MOKE arising from a thin-film NiO/Bi_2Se_3 heterolayer structure displays very interesting physical properties with potentially important device applications. Experimentally measurable Kerr rotations arise in the AFM/TI structure even though neither the AFM nor the TI have any net magnetization. The collinear g-type AFM's proximity to one of the TI surfaces leads to the breaking of both time-reversal symmetry and inversion symmetry. This results in a small but observable MOKE signature. The polar MOKE geometry is best suited for observing this effect, since the light is incident on the AFM/TI interface. This small MOKE can be enhanced by 5 orders of magnitude by optimizing the AFM and TI film thicknesses, which leads to a cavity resonance condition where the AFM and the substrate form a natural cavity. For slightly off-resonant structures, a 6° Kerr rotation can be obtained by varying the Fermi energy. This is encouraging for practical low-power devices as the Fermi energy has to be varied by less than 20 meV. We further show that this simple structure is resilient to 5% material growth error. Overall this can lead to practical low-power spintronics, fast electro-optic switches, magneto-optic memory, and gate-controlled optical isolators. This device is simple to grow, there is no magnetic doping required, it is planar, compact, and free of stray magnetic magnetization and external magnets.

ACKNOWLEDGMENTS

This work is supported as part of Spins and Heat in Nanoscale Electronic Systems (SHINES) an Energy Frontier Research Center funded by the U.S. Department of Energy, Office of Science, Basic Energy Sciences under Award No. DE-SC0012670.

[1] I. V. Kukushkin and V. B. Timofeev, Magneto-optics of strongly correlated two-dimensional electrons in single heterojunctions, Adv. Phys. **45**, 147 (1996).

[2] Yuval Ronen, Yonatan Cohen, Daniel Banitt, Moty Heiblum, and Vladimir Umansky, Robust integer and fractional helical modes in the quantum hall effect, Nat. Phys. **14**, 411 (2018).

[3] Wang-Kong Tse and A. H. MacDonald, Giant Magneto-Optical Kerr Effect and Universal Faraday Effect in Thin-Film Topological Insulators, Phys. Rev. Lett. **105**, 057401 (2010).

[4] Wang-Kong Tse and A. H. MacDonald, Magneto-optical faraday and kerr effects in topological insulator films and in other layered quantized hall systems, Phys. Rev. B **84**, 205327 (2011).

[5] Marc Serra-Garcia, Valerio Peri, Roman Süsstrunk, Osama R. Bilal, Tom Larsen, Luis Guillermo Villanueva, and Sebastian D. Huber, Observation of a phononic quadrupole topological insulator, Nature **555**, 342 (2018).

[6] Roberta Sessoli, Marie-Emmanuelle Boulon, Andrea Caneschi, Matteo Mannini, Lorenzo Poggini, Fabrice Wilhelm, and Andrei Rogalev, Strong magneto-chiral dichroism in a paramagnetic molecular helix observed by hard X-rays, Nat. Phys. **11**, 69 (2015).

[7] Mircea Vomir, Robin Turnbull, Ipek Birced, Pedro Parreira, Donald A. MacLaren, Stephen L. Lee, Pascal André, and Jean-Yves Bigot, Dynamical torque in $Co_xFe_{3-x}O_4$ nanocube thin films characterized by femtosecond magneto-optics: A π-shift control of the magnetization precession, Nano Lett. **16**, 5291 (2016).

[8] Wanjun Jiang, Xichao Zhang, Guoqiang Yu, Wei Zhang, Xiao Wang, M. Benjamin Jungfleisch, John E. Pearson, Xuemei Cheng, Olle Heinonen, Kang L. Wang, *et al.*, Direct observation of the skyrmion Hall effect, Nat. Phys. **13**, 162 (2016).

[9] Seonghoon Woo, Kyung Mee Song, Xichao Zhang, Yan Zhou, Motohiko Ezawa, Xiaoxi Liu, S. Finizio, J. Raabe, Nyun Jong Lee, Sang-Il Kim, *et al.*, Current-driven dynamics and inhibition of the skyrmion Hall effect of ferrimagnetic skyrmions in GdFeCo films, Nat. Commun. **9**, 959 (2018).

[10] Wanjun Jiang, Xichao Zhang, Guoqiang Yu, Wei Zhang, Xiao Wang, M. Benjamin Jungfleisch, John E. Pearson, Xuemei Cheng, Olle Heinonen, Kang L. Wang, Yan Zhou, Axel Hoffmann, and Suzanne G. E. te Velthuis, Direct observation of the skyrmion Hall effect, Nat. Phys. **13**, 162 (2017).

[11] Tonmoy K. Bhowmick, Amrit De, and Roger K. Lake, High figure of merit magneto-optics from interfacial skyrmions on topological insulators, Phys. Rev. B **98**, 024424 (2018).

[12] T. Arima, Magneto-electric optics in non-centrosymmetric ferromagnets, J. Phys.: Condens. Matter **20**, 434211 (2008).

[13] Evangelos Atmatzakis, Nikitas Papasimakis, Vassili Fedotov, Guillaume Vienne, and Nikolay I. Zheludev, Magneto-optical response in bimetallic metamaterials, Nanophotonics **7**, 199 (2018).

[14] P. Hansen, Magneto-optical recording materials and technologies, J. Magn. Magn. Mater. **83**, 6 (1990).

[15] Yoshishige Suzuki, Toshikazu Katayama, Sadafumi Yoshida, Kazunobu Tanaka, and Katsuaki Sato, New Magneto-Optical Transition in Ultrathin Fe(100) Films, Phys. Rev. Lett. **68**, 3355 (1992).

[16] M. Mansuripur, The magneto-optical kerr effect, Opt. Photonics News **11**, 34 (2000).

[17] P. Němec, M. Fiebig, T. Kampfrath, and A. V. Kimel, Antiferromagnetic opto-spintronics, Nat. Phys. **14**, 229 (2018).

[18] B. M. Lairson and B. M. Clemens, Enhanced magneto-optic kerr rotation in epitaxial PtFe (001) and PtCo (001) thin films, Appl. Phys. Lett. **63**, 1438 (1993).

[19] P. G. Van Engen, K. H. J. Buschow, R. Jongebreur, and M. Erman, Ptmnsb, a material with very high magneto-optical kerr effect, Appl. Phys. Lett. **42**, 202 (1983).

[20] K. Egashira and T. Yamada, Kerr-effect enhancement and improvement of readout characteristics in MnBi film memory, J. Appl. Phys. **45**, 3643 (1974).

[21] W. Reim and D. Weller, Kerr rotation enhancement in metallic bilayer thin films for magneto-optical recording, Appl. Phys. Lett. **53**, 2453 (1988).

[22] R. A. Duine, Kyung-Jin Lee, Stuart S. P. Parkin, and M. D. Stiles, Synthetic antiferromagnetic spintronics, Nat. Phys. **14**, 217 (2018).

[23] R. Pittini, J. Schoenes, O. Vogt, and P. Wachter, Discovery of 90° Magneto-Optical Polar Kerr Rotation in CeSb, Phys. Rev. Lett. **77**, 944 (1996).

[24] Peter Wadley, Bryn Howells, J. Železnỳ, Carl Andrews, Victoria Hills, Richard P. Campion, Vit Novák, K. Olejník, F. Maccherozzi, S. S. Dhesi, *et al.*, Electrical switching of an antiferromagnet, Science **351**, 587 (2016).

[25] Tomas Jungwirth, X. Marti, P. Wadley, and J. Wunderlich, Antiferromagnetic spintronics, Nat. Nanotechnol. **11**, 231 (2016).

[26] V. Baltz, A. Manchon, M. Tsoi, T. Moriyama, T. Ono, and Y. Tserkovnyak, Antiferromagnetic spintronics, Rev. Mod. Phys. **90**, 015005 (2018).

[27] Sang-Wook Cheong, Manfred Fiebig, Weida Wu, Laurent Chapon, and Valery Kiryukhin, Seeing is believing: Visualization of antiferromagnetic domains, npj Quantum Mater. **5**, 1 (2020).

[28] Igor Dzyaloshinsky, A thermodynamic theory of "weak" ferromagnetism of antiferromagnetics, J. Phys. Chem. Solids **4**, 241 (1958).

[29] Tôru Moriya, Anisotropic superexchange interaction and weak ferromagnetism, Phys. Rev. **120**, 91 (1960).

[30] V. Saidl, P. Němec, P. Wadley, V. Hills, R. P. Campion, V. Novák, K. W. Edmonds, F. Maccherozzi, S. S. Dhesi, B. L. Gallagher, *et al.*, Optical determination of the néel vector in a cumnas thin-film antiferromagnet, Nat. Photonics **11**, 91 (2017).

[31] Tomoya Higo, Huiyuan Man, Daniel B. Gopman, Liang Wu, Takashi Koretsune, Olaf M. J. van't Erve, Yury P. Kabanov, Dylan Rees, Yufan Li, Michi-To Suzuki, *et al.*, Large magneto-optical kerr effect and imaging of magnetic octupole domains in an antiferromagnetic metal, Nat. Photonics **12**, 73 (2018).

[32] Satoru Nakatsuji, Naoki Kiyohara, and Tomoya Higo, Large anomalous Hall effect in a non-collinear antiferromagnet at room temperature, Nature **527**, 212 (2015).

[33] M.-T. Suzuki, Takashi Koretsune, Masayuki Ochi, and Ryotaro Arita, Cluster multipole theory for anomalous hall effect in antiferromagnets, Phys. Rev. B **95**, 094406 (2017).

[34] Mingxing Wu, Hironari Isshiki, Taishi Chen, Tomoya Higo, Satoru Nakatsuji, and YoshiChika Otani, Magneto-optical kerr effect in a non-collinear antiferromagnet Mn_3Ge, Appl. Phys. Lett. **116**, 132408 (2020).

[35] Xiaodong Zhou, Wanxiang Feng, Xiuxian Yang, Guang-Yu Guo, and Yugui Yao, Electrically controllable crystal chirality magneto-optical effects in collinear antiferromagnets, ArXiv:2012.06693 (2020).

[36] Wenbo Wang, Julia A. Mundy, Charles M. Brooks, Jarrett A. Moyer, Megan E. Holtz, David A. Muller, Darrell G. Schlom, and Weida Wu, Visualizing weak ferromagnetic domains in multiferroic hexagonal ferrite thin film, Phys. Rev. B **95**, 134443 (2017).

[37] Richarj Mondal, Yuta Saito, Yuki Aihara, Paul Fons, Alexander V. Kolobov, Junji Tominaga, Shuichi Murakami, and Muneaki Hase, A cascading nonlinear magneto-optical effect in topological insulators, Sci. Rep. **8**, 1 (2018).

[38] Shreyas Patankar, J. P. Hinton, Joel Griesmar, J. Orenstein, J. S. Dodge, Xufeng Kou, Lei Pan, Kang L. Wang, A. J. Bestwick, E. J. Fox, D. Goldhaber-Gordon, Jing Wang, and Shou-Cheng Zhang, Resonant magneto-optic kerr effect in the magnetic topological insulator $Cr : (Sb_x, Bi_{1-x})_2Te_3$, Phys. Rev. B **92**, 214440 (2015).

[39] Murong Lang, Mohammad Montazeri, Mehmet C. Onbasli, Xufeng Kou, Yabin Fan, Pramey Upadhyaya, Kaiyuan Yao, Frank Liu, Ying Jiang, Wanjun Jiang, *et al.*, Proximity induced high-temperature magnetic order in topological insulator-ferrimagnetic insulator heterostructure, Nano Lett. **14**, 3459 (2014).

[40] Nikhil Sivadas, Satoshi Okamoto, and Di Xiao, Gate-Controllable Magneto-Optic Kerr Effect in Layered Collinear Antiferromagnets, Phys. Rev. Lett. **117**, 267203 (2016).

[41] Chao-Xing Liu, Xiao-Liang Qi, HaiJun Zhang, Xi Dai, Zhong Fang, and Shou-Cheng Zhang, Model hamiltonian for topological insulators, Phys. Rev. B **82**, 045122 (2010).

[42] Yongxin Zeng, Chao Lei, Gaurav Chaudhary, and Allan H. MacDonald, Quantum anomalous hall majorana platform, Phys. Rev. B **97**, 081102 (2018).

[43] C. S. Wang and J. Callaway, Band structure of nickel: Spin-orbit coupling, the fermi surface, and the optical conductivity, Phys. Rev. B **9**, 4897 (1974).

[44] H. Ebert, Magneto-optical effects in transition metal systems, Rep. Prog. Phys. **59**, 1665 (1996).

[45] M. Eddrief, F. Vidal, and B. Gallas, Optical properties of Bi_2Se_3: From bulk to ultrathin films, J. Phys. D: Appl. Phys. **49**, 505304 (2016).

[46] A. De and A. Puri, Cyclotron frequency coupled enhancement of kerr rotation in low refractive index-dielectric/magneto-optic bilayer thin-film structures, J. Appl. Phys. **91**, 9777 (2002).

[47] Petros N. Argyres, Theory of the Faraday and Kerr effects in ferromagnetics, Phys. Rev. **97**, 334 (1955).

[48] H. Feil and C. Haas, Magneto-Optical Kerr Effect, Enhanced by the Plasma Resonance of Charge Carriers, Phys. Rev. Lett. **58**, 65 (1987).

[49] A. De and A. Puri, Application of plasma resonance condition for prediction of large kerr effects, J. Appl. Phys. **92**, 5401 (2002).

[50] A. De and A. Puri, Kerr-resonance-condition-coupled enhancement in magneto-optic media, J. Appl. Phys. **93**, 1120 (2003).

[51] Masanori Abe and Takeshi Suwa, Surface plasma resonance and magneto-optical enhancement in composites containing multicore-shell structured nanoparticles, Phys. Rev. B **70**, 235103 (2004).

[52] S. Sriram and A. Thayumanavan, Structural, optical and electrical properties of NiO thin films prepared by low cost spray pyrolysis technique, Int. J. Mater. Sci. Eng. **1**, 118 (2013).

[53] *Handbook of Optical Constants of Solids*, edited by Edward D. Palik (Academic Press, London, 1998).